A time–frequency technique for the stability analysis of impulse responses from nonlinear aeroelastic systems

G. Dimitriadis*, J.E. Cooper

Manchester School of Engineering, University of Manchester, Oxford Road, Manchester M13 9PL, UK

Abstract

A time–frequency method is proposed for the analysis of response time histories from nonlinear aeroelastic systems. The approach is based on a time-varying curve-fit of the short time Fourier transform of the impulse response. It is shown that the method can be used in order to obtain a clear picture of the sub-critical stability of a number of aeroelastic systems with a variety of structural and aerodynamic nonlinearities. Additionally, frequency and amplitude information can be obtained for both the linear and nonlinear signatures of the response signals in the sub- and post-critical regions. Finally, it is shown that, given certain types of nonlinear functions, sub-critical damping trends can be extrapolated to predict bifurcation airspeeds.
© 2003 Elsevier Ltd. All rights reserved.

1. Introduction

The aerospace community is becoming increasingly aware of the importance of nonlinear aeroelastic phenomena in both civil and military aerospace applications. One of the major concerns is the characterization and prediction of the stability of aircraft in the presence of nonlinearities. The stability analysis of nonlinear aeroelastic systems is now being considered to be of crucial importance. Considerable effort is being devoted to the prediction of flutter and limit cycle oscillations for such systems using a variety of methods such as Centre Manifold Theory (Liu et al., 1999), Cell Mapping (Levitas et al., 1994), variants of the Harmonic Balance Method (Raghothama and Narayanan, 1999) etc. However, all these approaches assume that the system under investigation is fully determined, i.e. that its equations of motion are known. In practice, when an aircraft is tested (either on the ground or in flight), only its dynamic response to a given excitation signal is known. The effectiveness of identification methods for nonlinear systems is still problem-specific and, as a consequence, these techniques cannot in general be used to obtain the equations of motion of the aircraft. Hence, there is a need for methodologies which can predict the stability of nonlinear aeroelastic systems from response data.

Mastroddi and Bettoli (1999) analysed the output signal of a nonlinear system in the neighbourhood of a Hopf bifurcation using wavelets in order to separate the linear and nonlinear signatures of the signal. They showed that this decomposition can be used to estimate the critical airspeed from sub-critical data. However, the method is only rigorous in the neighbourhood of a Hopf bifurcation.

In this work an alternative time–frequency approach is introduced which is valid throughout the sub-critical region, even far away from the Hopf point. The new methodology is based on a time-varying curve-fit of the short time Fourier transform (STFT) of the response of a nonlinear aeroelastic system, which, for a large class of nonlinearities, allows the identification of all the harmonic components (linear and nonlinear) present in the motion. By following the evolution

---

*Corresponding author. Tel.: +44-161-275-4411.

E-mail address: grigorios.dimitriadis@man.ac.uk (G. Dimitriadis).

of these components in time and their variation with airspeed the stability of the system can be assessed up to the point of a critical bifurcation (either to flutter or to limit cycle oscillations).

The feasibility of using time-varying curve-fits is demonstrated initially on a single-degree-of-freedom (dof) nonlinear dynamic system. Then, the proposed method is formulated for multi-dof systems and applied to two simulated nonlinear aeroelastic systems with a variety of nonlinearities and aerodynamic formulations.

2. Equivalence of time-varying linear and nonlinear systems

The aim of this section is to demonstrate the equivalence between a nonlinear and a time-varying linear system and thus to justify the use of STFT techniques. Consider a simple 1-dof nonlinear system with cubic stiffness. The unforced equation of motion is given by

$$M\ddot{y} + C\dot{y} + K_1 y + K_2 y^3 = 0, \tag{1}$$

where y is the displacement, M is the mass, C the damping coefficient, K_1 the linear stiffness coefficient and K_2 the cubic stiffness coefficient. Eq. (1) can be written in a more concise form as

$$M\ddot{y} + C\dot{y} + K(y)y = 0, \tag{2}$$

where $K(y) = K_1 + K_2 y^2$ can be referred to as the *nonlinear stiffness function*. The basic idea underlying the process of linearization using time-variable linear systems is that Eq. (2) can be expressed as

$$M\ddot{y} + C\dot{y} + \hat{K}(t)y = 0, \tag{3}$$

where $\hat{K}(t)$ is independent of $y(t)$. However, since the character of the response of nonlinear systems depends on initial conditions (in this case $y(0)$ and $\dot{y}(0)$), the function $\hat{K}(t)$ must also depend on these initial conditions. Hence $\hat{K} = \hat{K}(t, y(0), \dot{y}(0))$.

Going back to Eq. (2), it can be seen that as y tends to zero, $\lim_{y\to 0} K(y) = K_1$, in other words, as the response level decreases, the system becomes increasingly linear. Additionally, if $C > 0$ and there are no external forces applied on the system, $\lim_{t\to\infty} y(t) = 0$. Hence, it can be deduced that $\lim_{t\to\infty} K(y) = K_1$. In the case where $C < 0$, $\lim_{t\to\infty} y(t) = \infty$ and $\lim_{t\to\infty} K(y) = \infty$. The case $C = 0$ yields a bounded $y(t)$ and, hence, no judgement can be made for the value of $\lim_{t\to\infty} K(y)$.

In order to perform time-variable linearization on Eq. (2), a function $\hat{K} = \hat{K}(t, y(0), \dot{y}(0))$ must be sought which has the following characteristics:

$$\hat{K}(0) = K_1 + K_2 y^2(0), \tag{4}$$

$$\lim_{t\to\infty} \hat{K}(t) = K_1 \;\; \text{if} \;\; C > 0,$$
$$\lim_{t\to\infty} \hat{K}(t) = \infty \;\; \text{if} \;\; C < 0. \tag{5}$$

Therefore, the values of $\hat{K}$ are known for $t = 0$ and ∞, but nothing is known about the behaviour of the function at all other times. Fig. 1 shows the free response of the nonlinear system with initial condition $y(0) = 0.3$ m and $M = 1.2$ kg, $C = 1.52$ N s/m, $K_1 = 210$ N/m, $K_2 = 35\,200$ N/m^3. The shape of the response is that of an exponentially decaying sinusoid with decreasing frequency. The variation of frequency with time can be calculated from the zero crossings of the response signal. If the time coordinate of the nth zero crossing of y(t) is denoted by $t_0(n)$ then the frequency variation is given by

$$f(t_0(n)) = \frac{1}{t_0(n) - t_0(n-1)}. \tag{6}$$

This function is plotted in Fig. 2. It can be seen that the function has a nonzero value at $t = 0$ and asymptotes to a finite value as $t \to \infty$. Hence, it is a very good candidate for $\hat{K}$. Indeed, from basic dynamical theory, the frequency of a single-dof oscillator is given by $2\pi f = \sqrt{(K/M)}$. Substituting $\hat{K}$ we get

$$\hat{K} = M(2\pi f)^2. \tag{7}$$

This function is plotted in Fig. 3. It asymptotes to K_1 as $t \to \infty$ and its initial value is approximately equal to $K_1 + K_2 y^2(0)$. Hence, according to the conditions of Eq. (5), this function is a suitable choice for $\hat{K}$, for the particular case where the initial condition is $y(0) = 0.3$. The same form of function would be suitable for a system in which $C < 0$. By substituting back into Eq. (3) and numerically integrating the system, the response of the linearized, time-varying system can be obtained. In Fig. 4, the responses of the nonlinear and linearized systems are plotted on the same axes,
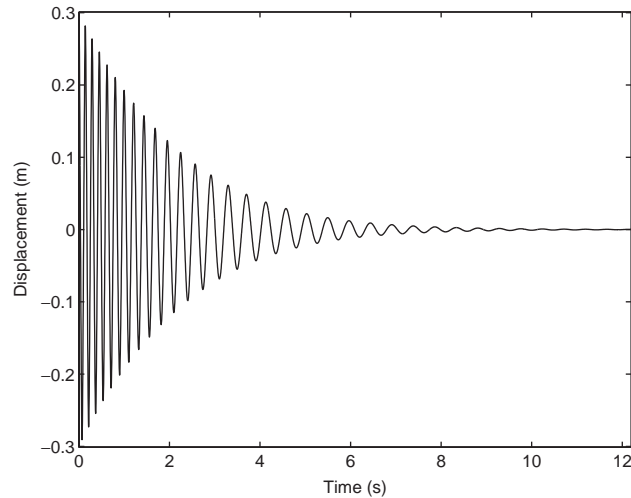
Fig. 1. Response of 1-dof system with cubic stiffness, $y(0) = 0.5$.
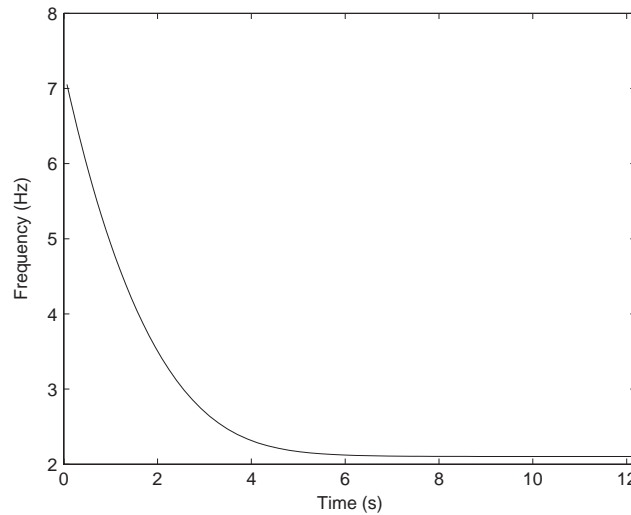
Fig. 2. Frequency variation with time.

showing that the agreement between the two signals is quite good. This result demonstrates the feasibility of the concept of approximating nonlinear system impulse responses by impulse responses from equivalent linear time-varying systems.

3. Time and frequency curve-fit for multi-dof nonlinear systems

In the previous section, it was shown that the response signal of a single-dof nonlinear dynamic system can be adequately curve-fitted using an exponentially decaying sinusoid whose frequency varies with time. In this section, the same rationale is applied to multi-dof nonlinear systems and an original methodology for a 'time and frequency' domain curve-fit is developed. A curve-fit of the system impulse response in the frequency domain is followed by a signal reconstruction in the time domain. The process is akin to curve-fitting the *STFT* (Allen and Rabiner, 1977) of the response signal. The STFT is given by

$$STFT(\tau, \omega) = \int_{\tau - t_1}^{\tau + t_1} w(t - \tau) H(t) e^{-j\omega t} \, dt, \tag{8}$$
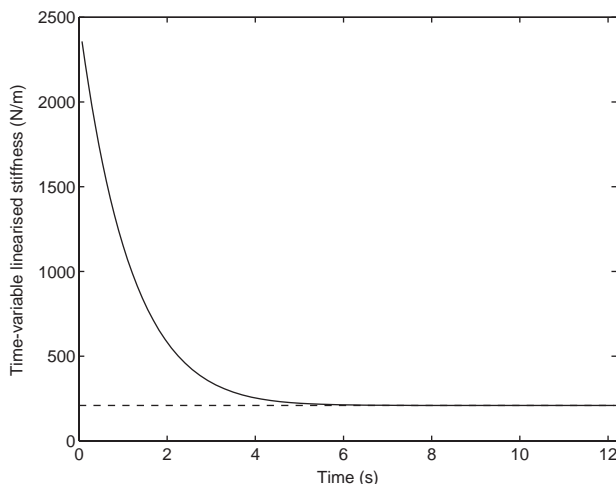
Fig. 3. Linearized, time-varying stiffness function variation with time.
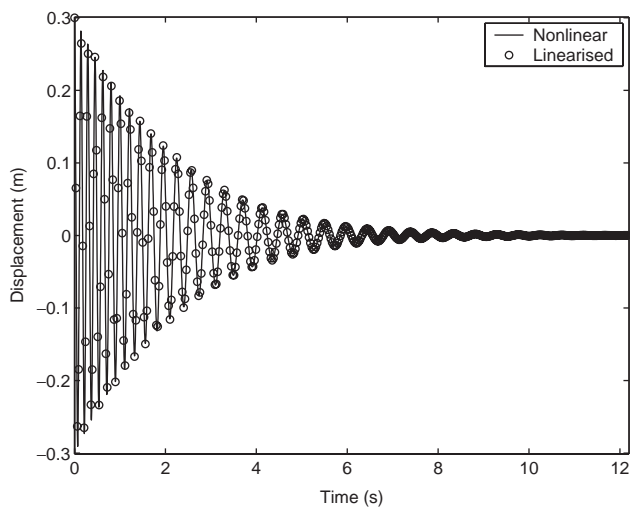
Fig. 4. Comparison of responses from nonlinear and linearized, time-varying system.

where τ is the time instance at which the response is Fourier transformed, t_1 is equal to half the length of the response section that is Fourier transformed (for the case of a section with 1028 points, $t_1 = 1028\Delta t/2$) and $w(t)$ is a 'sliding window' function which, in this case, is rectangular, i.e. $w(t) = 1$.

The time and frequency parts of the methodology are presented in separate subsection. In the rest of this paper, the term *impulse response* will be used to denote the time domain response of a system to an initial displacement and the term frequency response function (FRF) will denote the Fourier transform of the impulse response.

3.1. Frequency domain curve-fit

The technique used in the previous section to estimate the frequency variation with time cannot be applied to a multi-dof system because the response of such a system will, in general, contain more than one frequency at any one time. Hence, a more sophisticated approach is followed, based on the rational fraction polynomial (RFP) method (Richardson and Formenti, 1982).

The standard RFP method (Géradin and Rixen, 1997) attempts to express the FRF of a given dynamic system in terms of a polynomial fraction of the form

$$H(\omega) = \frac{b_{nb}(j\omega)^{nb} + b_{nb-1}(j\omega)^{nb-1} + \cdots + b_0}{(j\omega)^{na} + a_{na-1}(j\omega)^{na-1} + \cdots + a_0} + \varepsilon, \tag{9}$$

where $H(\omega)$ is the FRF, b_i, a_i are the coefficients of the polynomials, nb and na are the orders of the polynomials and ε is the error. Then, b_i, a_i are evaluated in a least-squares sense by rewriting Eq. (9) as

$$\begin{Bmatrix} H(\omega_1)(j\omega_1)^{na} \\ H(\omega_2)(j\omega_2)^{na} \\ \vdots \\ H(\omega_L)(j\omega_L)^{na} \end{Bmatrix} = - \begin{pmatrix} H(\omega_1)(j\omega_1)^{na-1} & H(\omega_1)(j\omega_1)^{na-2} & \dots & H(\omega_1) \\ H(\omega_2)(j\omega_2)^{na-1} & H(\omega_2)(j\omega_2)^{na-2} & \dots & H(\omega_2) \\ \vdots & \vdots & \vdots & \vdots \\ H(\omega_L)(j\omega_L)^{na-1} & H(\omega_L)(j\omega_L)^{na-2} & \dots & H(\omega_L) \end{pmatrix}$$

$$\times \begin{Bmatrix} a_{na-1} \\ a_{na-2} \\ \vdots \\ a_0 \end{Bmatrix} + \begin{pmatrix} (j\omega_1)^{nb} & (j\omega_1)^{nb-1} & \dots & 1 \\ (j\omega_2)^{nb} & (j\omega_2)^{nb-1} & \dots & 1 \\ \vdots & \vdots & \vdots & \vdots \\ (j\omega_L)^{nb} & (j\omega_L)^{nb-1} & \dots & 1 \end{pmatrix} \begin{Bmatrix} b_{nb} \\ b_{nb-1} \\ \vdots \\ b_0 \end{Bmatrix} + \text{Error terms} \tag{10}$$

which is equivalent to the form $\mathbf{Y} = -\boldsymbol{\Phi}_a \mathbf{a} + \boldsymbol{\Phi}_b \mathbf{b}$. Finally, b_i, a_i are obtained by writing Eq. (10) as

$$\mathbf{Y} = \begin{pmatrix} -\boldsymbol{\Phi}_a & \boldsymbol{\Phi}_b \end{pmatrix} \begin{Bmatrix} \mathbf{a} \\ \mathbf{b} \end{Bmatrix} \tag{11}$$

and solving in a least-squares sense.

Traditionally, the coefficients a_i, b_i are forced to be real by solving the real and imaginary parts of Eq. (11) separately while choosing $na = 2 \times m$, where m is the number of modes in the system. Then, the roots of the denominator are m complex conjugate pairs and are also the eigenvalues of the system.

For the present work, a slightly modified approach is introduced. The coefficients of both the numerator and the denominator are allowed to be complex. Additionally, the requirement that $na = 2 \times m$ is relaxed. Since the technique is to be used on response signals from nonlinear systems, the eigenvalues will not necessarily be pairs of complex conjugate numbers. Consequently, an optimization procedure is employed to obtain na and nb so that both polynomials will have the number of terms required in order to adequately fit the signal. The optimization procedure searches for the values of na and nb which minimize $|\mathbf{Y} + \boldsymbol{\Phi}_a \mathbf{a} - \boldsymbol{\Phi}_b \mathbf{b}|^2$. The upper limits of the possible values of na and nb are obtained from the criterion that $[-\boldsymbol{\Phi}_a \quad \boldsymbol{\Phi}_b]$ should not be rank-deficient.

The eigenvalues are given by the roots of the denominator. In this approach, the roots are not complex conjugate pairs. Hence, the RFP method models the three-dimensional landscape that is described by $H(\omega)$ in the real–imaginary–frequency space.

The RFP approach cannot be used to curve-fit an entire impulse response from a nonlinear system in one application, since the frequencies and dampings of the impulse response will change with time. Hence, the impulse response must be split into small section, and the RFP method must be applied to each section separately. The length of each section is determined mainly by two factors: (i) the rate at which the strongly nonlinear part of the response decays; (ii) the desired time and frequency resolution.

For many nonlinear functions, the impulse response of a stable nonlinear system is highly nonlinear at high amplitudes but tends to linear as the amplitude tends to zero. Hence, the strongly nonlinear part of the impulse response needs to be subdivided into relatively small section the purposes of RFP curve-fitting in order to capture the variation of frequency components with time. The approximately linear, low amplitude part of the response can be curve-fitted using a single section. The impulse response of a nonlinear system which undergoes limit cycles features a nonlinear transient part, followed by the LCO behaviour. Again, the transient part needs to be curve-fitted in small section while the LCO part can be treated as quasi-linear and curve-fitted as a single section. In this sense, the RFP curve-fit is a multi-resolution approach, but not in the same sense as the wavelet transform where the resolution is uniquely dependent upon the value of the central response frequency (Heil and Walnut, 1989). It should be stressed that this description of nonlinear impulse responses only holds for some nonlinearities. As will be shown later, in the case of freeplay, the response is strongly nonlinear at low amplitudes and needs to be subdivided into small section throughout the duration of the impulse response.

3.2. Signal reconstruction in the time domain

After the eigenvalues are evaluated for each section using the RFP technique, they are used to reconstruct the time-domain signal using

$$y(t) = y_f(t) + \varepsilon, \tag{12}$$

where $y(t)$ is the true signal and $y_f(t)$ is a sum of exponentially decaying sinusoids given by

$$y_f(t) = \sum_{i=1}^{na} A_i \exp\left(-\mathfrak{R}(\lambda_i)t\right) \cos \mathscr{I}(\lambda_i)t + B_i \exp\left(-\mathfrak{R}(\lambda_i)t\right) \sin \mathscr{I}(\lambda_i)t + C; \tag{13}$$

$\mathfrak{R}$ and $\mathscr{I}$ denote real and imaginary parts, respectively, and A_i, B_i, C are unknown coefficients to be determined.

The purpose of the signal reconstruction is to determine the relative importance of each eigenvalue obtained from the application of the RFP approach. Some of the eigenvalues returned by the method act as residuals which improve the frequency curve-fit or accommodate noise but do not represent the dynamics of the signal in the chosen frequency band. In this sense, the frequency domain is used in order to identify candidate eigenvalues and the time domain is used to choose which of the candidates are significant. The system impulse response is curve-fitted using each eigenvalue separately to obtain values for the amplitudes $\bar{A}_i$ and $\bar{B}_i$ corresponding to the ith eigenvalue

$$y(t) = \bar{A}_i \exp^{-\mathfrak{R}(\lambda_i)t} \cos \mathscr{I}(\lambda_i)t + \bar{B}_i \exp^{-\mathfrak{R}(\lambda_i)t} \sin \mathscr{I}(\lambda_i)t + \bar{\varepsilon}. \tag{14}$$

The evaluation of $\bar{A}_i$ and $\bar{B}_i$ is performed in a least-squares sense, such that the square of the difference between the true and curve-fitted signals, $\bar{\varepsilon}^2$, is minimized. The total amplitudes $\sqrt{\bar{A}_i^2 + \bar{B}_i^2}$ are sorted in descending order of magnitude and the sorting index is used to sort the corresponding eigenvalues in descending order of importance. Let k be the sorting index such that $k = 1$ denotes the most important eigenvalue and $k = na$ the least important one. Then, the following curve-fits are performed:

$$y(t) = y_{fk}(t) + \varepsilon_k, \tag{15}$$

where $k = 1, .., na$, and

$$y_{fk}(t) = \sum_{i=1}^{k} A_{ik} \exp\left(-\mathfrak{R}(\lambda_i)t\right) \cos \mathscr{I}(\lambda_i)t + B_{ik} \exp\left(-\mathfrak{R}(\lambda_i)t\right) \sin \mathscr{I}(\lambda_i)t + C, \tag{16}$$

C being the mean value of $y(t)$. For each value of k the amplitudes A_{ik} and B_{ik} are obtained in a least-squares sense and an error reduction ratio (ERR) for a curve-fit using k eigenvalues is defined as

$$ERR_k = \text{std}\left(y_{fk}(t) - y(t)\right), \tag{17}$$

where std denotes the standard deviation. The minimum value of the error reduction ratio chosen for this study was $ERR > 0.01$ which was found adequate in order to exclude all the residual eigenvalues. Then, if λ_p is the last eigenvalue for which $ERR_p > 0.01$, the final time-domain curve fit is given by $y_{fp}(t)$ and the significant eigenvalues are λ_k for $k = 1, \ldots, p$.

4. Applications of time-varying RFP method to simulated nonlinear aeroelastic systems

In this section, the RFP methodology is applied to two simulated nonlinear aeroelastic models: (i) the Hancock model with control surface, which is a 3-dof model of a rigid wing with control surface in an incompressible airflow; (ii) a CFD model of a 2-dof airfoil in transonic flow.

A detailed description of the Hancock system with control surface is given by Dimitriadis and Cooper (1999). For convenience, the system will be referred to as the Hancock model, even though the original Hancock model (Hancock et al., 1985) does not feature a control surface. Fig. 5 shows the layout of the model. The wing is a rectangular flat plate with chord length c and span s. Structural stiffness is provided by three springs, K_γ, K_θ and K_β, in the heave, γ, pitch, θ and control surface pitch, β, degrees of freedom. The airfoil pitches around the flexural axis, situated at x_f and the control surface rotates around the hinge axis, denoted by x_h. The aerodynamics are modelled using quasi-steady strip theory with approximations for some of the unsteady aerodynamic derivatives. The Hancock model can feature a stiffness nonlinearity in the control surface degree of freedom. The nonlinear functions considered in this work are cubic and freeplay and are plotted in Fig. 6.

The CFD model used in this study, is a structural model of a 2-dof NACA0012 airfoil (Lee et al., 1999). Fig. 7 shows a drawing of the airfoil, suspended from two springs, K_h and K_α, providing stiffness in pitch, α, and plunge, h,
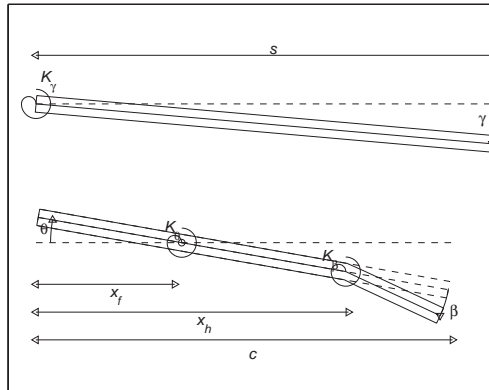
Fig. 5. The Hancock model with control surface.
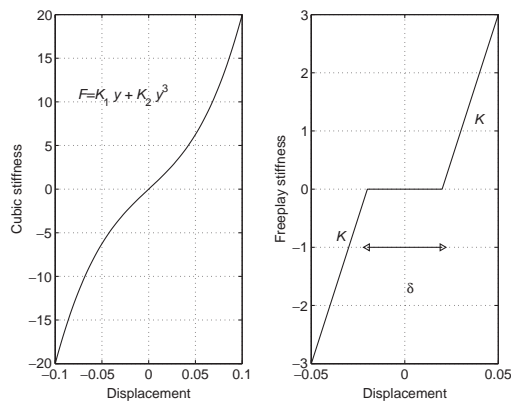
Fig. 6. Nonlinear functions applied to the Hancock model.
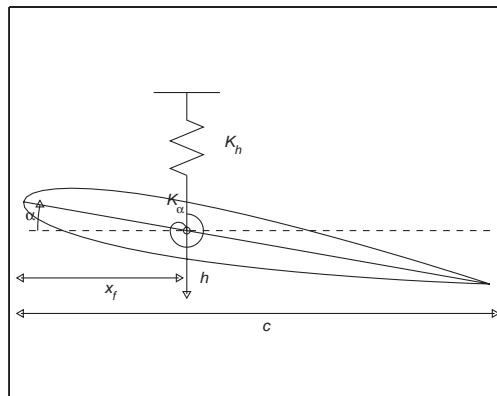
Fig. 7. 2-D NACA 0012 airfoil used for transonic CFD calculations.

respectively. The airfoil has a chord of length c and is pitching around its flexural axis, which is located at x_f. This structural model is coupled with transonic aerodynamic forces obtained from the solution of the Euler equations. The solution is obtained by means of the PMB 2D code, developed at the Department of Aerospace Engineering of Glasgow University. The theoretical basis of this code can be found in Badcock et al. (1995) and some more recent applications are detailed in Goura et al. (2001a, b). Fig. 8 shows the computational grid used to solve the Euler equations. The grid
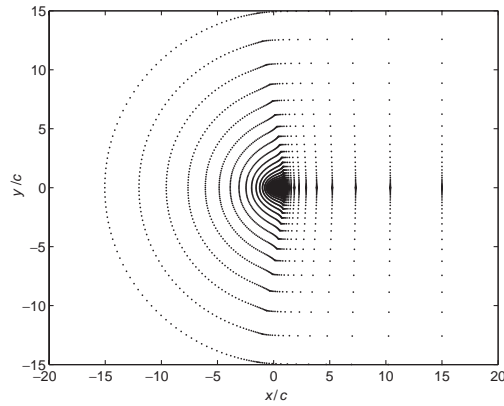
Fig. 8. Solution grid for NACA0012 CFD calculations.
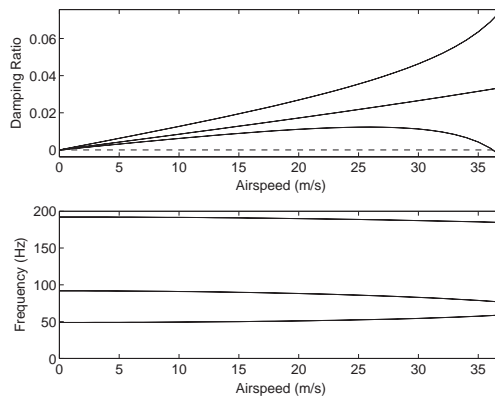
Fig. 9. Damping ratio and natural frequency variation for the linear Hancock model.
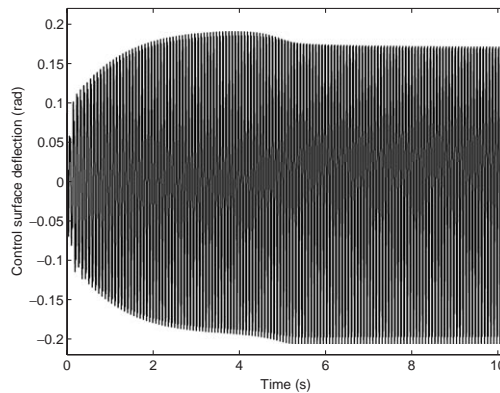
Fig. 10. Control surface impulse response with cubic nonlinearity for an airspeed of 50 m/s.

has a radius of 15 chord lengths and includes a wake of 14 chord lengths. The nonlinearity in this case is entirely due to the transonic aerodynamics.

4.1. Hancock model with cubic stiffness

In this example, the time-varying RFP technique is applied to the Hancock model with cubic stiffness. Before any nonlinear results are presented, it is useful to discuss the stability of the Hancock model in the absence of nonlinearity.

Fig. 9 shows the variation of the natural frequencies and damping ratios of the Hancock wing with airspeed. The critical damping curve is the control surface damping ratio which goes to zero at 36.5 m/s indicating flutter. From the frequency plot, it can be seen that the three natural frequencies start off at approximately 8, 14 and 30 Hz. As the airspeed is increased, the 8 and 14 Hz components (control surface deflection and wing torsion respectively) approach each other, forming the flutter mechanism.

In Fig. 10 the control surface impulse response for the nonlinear case is plotted at an airspeed of 50 m/s. This result was obtained by integrating numerically the nonlinear aeroelastic model using 20 480 time steps of length 5×10^{-4} s. It can be seen that, at this particular airspeed the system undergoes a limit cycle oscillation (LCO). The STFT for the same response is shown in Fig. 11. The STFT was obtained by using time windows of 1024 time steps (i.e. 0.512 s). As the time domain response amplitude increases, the response frequencies also increase slightly. Approximately 4 s into the response, the system switches from a zero-mean limit cycle to one that is not centred around zero. The STFT shows that the new limit cycle has twice as many frequency components. After the LCO is stabilized, the frequencies remain constant.

The arithmetic values of all the frequency components in the STFT can be obtained by use of the time-varying RFP method. The curve-fit was performed using frequency data between 0 and 150 Hz from each STFT section. In order to obtain an accurate fit, the frequency range was split into 3 section and Eq. (10) was applied separately to each section. The resulting eigenvalues were then used in the time domain reconstruction. After the reconstruction, between 5 and 10 eigenvalues were retained at each response section. The frequencies obtained from these eigenvalues are plotted against time in Fig. 12. The high quality of the curve-fit obtained after the time domain signal reconstruction is demonstrated in Fig. 13, where the actual and curve-fitted time domain signals are plotted on the same axes for a portion of the response.

4.1.1. Stability analysis

The results presented up to now indicate that the time-varying RFP yields very good approximations of impulse responses from nonlinear signals. However, the most important characteristic of aeroelastic systems is the fact that their dynamic behaviour changes radically with airspeed, including bifurcations to LCOs and flutter. It will be demonstrated that the time-varying RFP curve-fit is a useful tool for tracking these changes from impulse response data and even for predicting imminent instabilities.

The changing character of the response of a nonlinear aeroelastic system with airspeed can be illustrated using a bifurcation diagram (Dimitriadis and Cooper, 2000). On a bifurcation plot, the response is plotted only at times when its derivative is zero and is, consequently, a type of amplitude plot. The plotting is repeated at a number of airspeeds, thus giving an overview of the dynamic behaviour of the system over a given speed range. At airspeeds where the response is decaying only zeros are plotted. The actual amplitude points are only plotted at airspeeds where the response is a LCO. The process of building up a bifurcation plot is more clearly explained with the following 'bifurcation function':

$$\mathscr{B}(V) = \begin{cases} 0 & \text{decay}, \\ y|_{\dot{y}=0} & \text{LCO}, \end{cases} \tag{18}$$

where V is the airspeed, $\mathscr{B}(V)$ is the bifurcation function, and y is the system response.

Before any results are presented, the concept of LCO period should be briefly discussed. This concept denotes the complexity of a LCO motion and was introduced into the aeroelastic community by papers such as Price et al. (1994) and Kim and Lee (1996). Essentially, a period-n LCO is a closed curve with n loops in the phase plane, as shown in Fig. 14. The higher the period number of the LCO, the higher its complexity. In Dimitriadis and Cooper (2000) the term period-x LCO was used to describe LCOs of such high complexity that they are quasi-periodic. Period-doubling and period-halving behaviour denotes a rapid increase or decrease in LCO complexity within a short airspeed range. Often, period doubling leads to period-x LCOs or even chaotic behaviour (Price et al., 1995).

Fig. 15 shows the bifurcation plot for the Hancock model with cubic stiffness. The results are summarized below:

- 0–37 m/s: the response is decaying;
- 38–42 m/s: the system admits a period-1 limit cycle;
- 42–48 m/s: the system undergoes period-doubling behaviour, i.e. successive bifurcations to higher period limit cycles (Dimitriadis and Cooper, 1999);
- 48–50 m/s: period-halving behaviour, i.e. bifurcations to lower period limit cycles;
- 50–53 m/s: period-4 limit cycle;
- 53–55 m/s: period-6 limit cycle;
- 55–57.5 m/s: period-doubling behaviour;
- > 57.5 m/s: flutter.
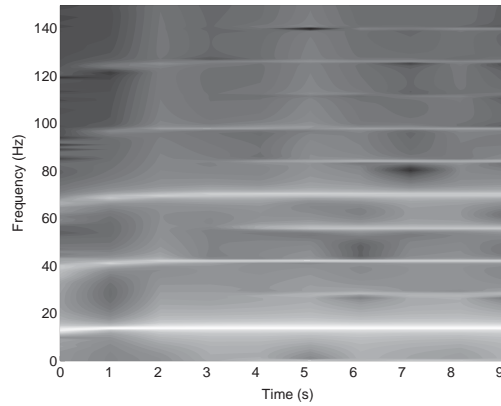
Fig. 11. Short time Fourier transform of response in Fig. 10.
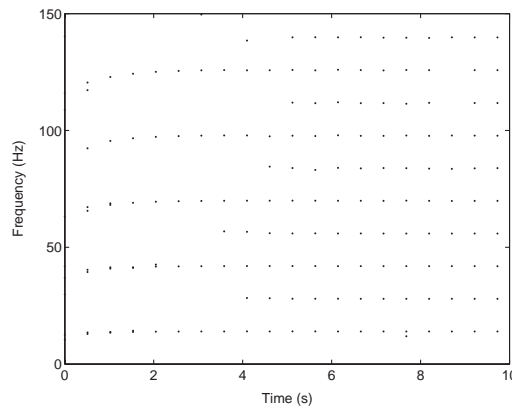
Fig. 12. Frequencies from RFP curve-fit of response in Fig. 10.
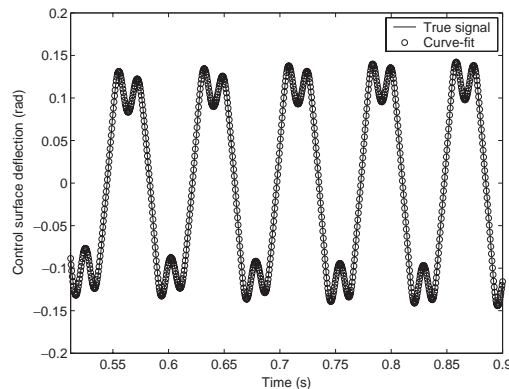
Fig. 13. Comparison of true and curve-fitted signals.

Note that LCOs first appear at an airspeed slightly higher than the linear flutter speed. The time-varying RFP curve fits can also be used to provide stability information over a range of airspeeds. This is achieved by performing curve fits at each individual airspeed and then plotting all the eigenvalues obtained from each fit against airspeed on two separate figures, one for the real part (or damping ratios) and one for the imaginary part (or natural frequencies). In Fig. 16 the damping ratios are plotted for the Hancock model with cubic stiffness. The shape of the figure at airspeeds below 37 m/s is very similar to the response of the linear 3-dof system, see Fig. 9. Three damping curves can be distinguished, the
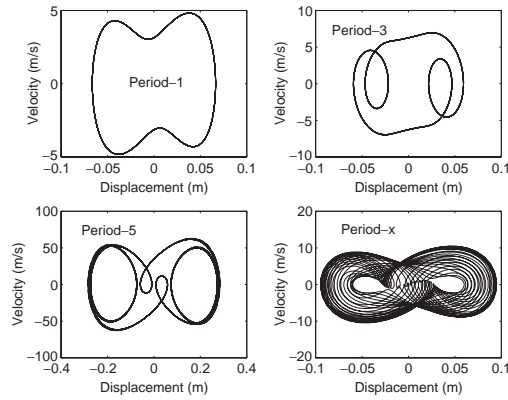
Fig. 14. LCOs of increasing complexity, demonstrating the concept of LCO period.
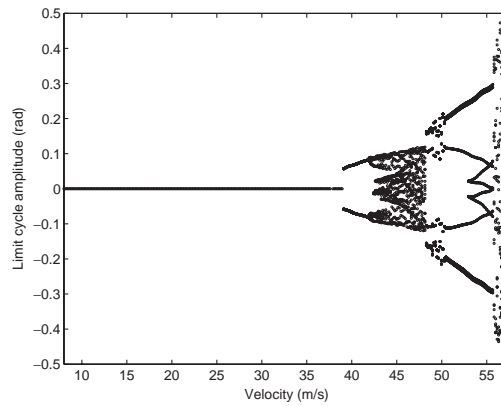
Fig. 15. Bifurcation plot for Hancock model with cubic stiffness.
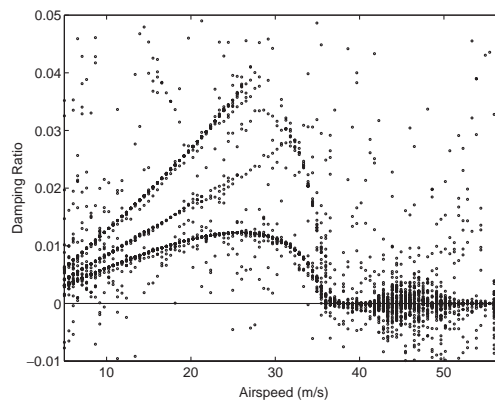
Fig. 16. Time-varying RFP damping plot for Hancock model with cubic stiffness.

lowest representing the damping of the motion of the control surface, the middle one represents the torsional wing vibrations and the top curve is due to the wing motion in bending. It should be noted here that positive damping ratios denote positive stability, i.e. decaying response. The behaviour of all three damping curves is of interest, as follows.

 (i) 15–37 m/s: The control surface damping curve is well-defined, its value starts off positive, increases slightly (up to approximately 26 m/s) and then decreases to zero. This is the region where the response is decaying and the control surface damping curve is behaving very much like a critical damping curve in a linear aeroelastic system. When the damping reaches zero, the system goes into limit cycle oscillations. After 30 m/s the wing torsion damping also starts to decrease towards zero. The wing bending damping curve seems to disappear at 26 m/s.

 (ii) 38–42 m/s: Only one prominent damping curve exists, centred around zero. The width of the damping curve is slowly increasing with airspeed. The bifurcation plot indicates that, in this region, the system undergoes period-1 LCOs. The widening of the PDC may well signify the fact that a new bifurcation is imminent

(iii) 42–48 m/s: The damping curve is considerably scattered over a large range of damping ratio values (positive and negative). The period-doubling behaviour causes very complex (period-x) LCOs whose frequencies and dampings change constantly with time. In order to curve-fit these responses using the RFP technique, a large number of eigenvalues with considerable scatter is required. In fact, the accuracy of the RFP is drastically reduced in this flight regime.

(iv) 48–55 m/s: The system bifurcates to low period LCOs so that the quality of the curve-fits improves considerably.

 (v) 55–57.5 m/s: The scatter in the damping ratios is again increased due to the period-doubling behaviour.

(vi) > 57.5 m/s: Flutter (deduced from the bifurcation diagram).

A note should be made of the fact that there is a considerable number of negative damping ratios which, in a linear system, would indicate instability. It should be remembered though that the RFP approach does not fit the nonlinear system; the eigenvalues obtained from the curve-fits reflect the response signal, modelled as the response of an equivalent time-varying linear system. Hence, it can happen that an eigenvalue with a positive real part (i.e. negative damping ratio) is needed in order to accurately fit a particular section of the response.

Fig. 17 plots the natural frequencies obtained from the application of the time-varying RFP procedure to the Hancock model with control surface. Its main features are the following.

 (a) 15–36 m/s: Four very prominent frequencies at 9, 15, 31 and 48 Hz are visible. The prominence of each frequency refers to how many times the frequency appears in the impulse response at a given airspeed. The 9 Hz frequency is the frequency of the control surface mode, the 15 Hz frequency corresponds to wing torsion and the 31 Hz to wing bending. The 48 Hz frequency component is a harmonic of the control surface with very small damping but also very little energy hence, it does not appear in the damping plots. From 30 m/s onwards, the 9 and 15 Hz frequency components start to merge. This is the linear flutter mechanism. However, the frequency components at 31 and 48 Hz also appear to draw closer to each other. It is not known whether this is a secondary instability mechanism. The low energy content of the 48 Hz component suggests that, if there is a second instability mechanism, its effect must be small.

 (b) 36–42 m/s: The system starts to limit cycle. The four frequencies of the previous region have merged into two components at 12 and 38 Hz. Two new prominent frequency components appear at 65 and 90 Hz and, later on, two
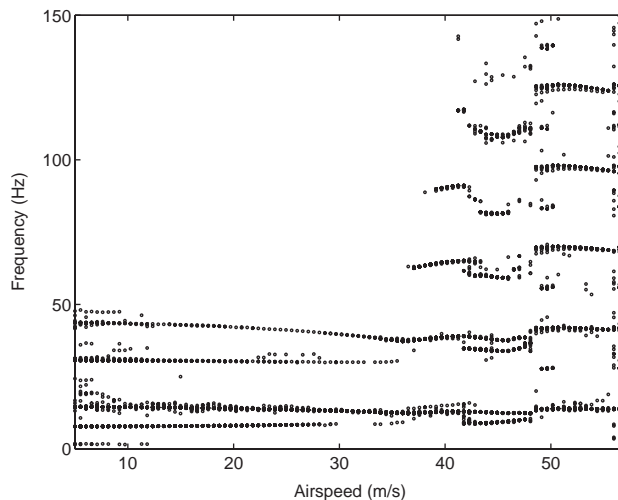
Fig. 17. Time-varying RFP frequency plot for Hancock model with cubic stiffness.

further frequencies appear at 117 and 142 Hz. All the new components are higher harmonics and accommodate the shape of the limit cycles.

(c) 42–48 m/s: In this speed range the system undergoes period doubling. There are now nine frequency components but these results are not trustworthy since, as mentioned earlier, the quality of the curve-fits in this region is mediocre.

(d) 48–56 m/s: All the frequency components become better defined, and the number of the frequency components rapidly drops from 10 to 6 as a result of the drop in the complexity of the LCOs.

(e) 56–57.5 m/s: Increased scatter in all of the frequency components.

(f) > 57.5 m/s: Flutter (deduced from the bifurcation diagram).

Figs. 16 and 17 demonstrate that it is possible to track the sub-critical stability of a multi-dof nonlinear aeroelastic system using time–frequency techniques. When at least one of the sub-critical damping curves decreases towards zero, it is a sign of impending instability.

4.1.2. Stability prediction from sub-critical data

Up to now it has been demonstrated that the application of the time-varying RFP method to response data from the Hancock model with cubic nonlinearity in the control surface can yield time-varying damping plots, such as the one in Fig. 16. These damping plots show clearly that the value of each damping curve becomes zero at the bifurcation point. In this section it will be shown that these damping curves can be unified into a single stability criterion that can be used to predict the bifurcation airspeed from sub-critical data.

Fig. 16 can only be used for a qualitative estimation of the system stability. However, by averaging the damping values obtained at each airspeed, a single damping curve can be obtained. This averaged damping curve also tends to zero at the bifurcation point.

In order to demonstrate the use of the averaged damping criterion in estimating the bifurcation speed from sub-critical data, the following simulated 'flutter test' was performed.

1. The system impulse response was simulated at 5 m/s and then at increasing airspeeds, at intervals of 2 m/s.
2. At each airspeed, the time-varying RFP method was used to obtain the averaged damping criterion.
3. At each airspeed, the current and previous damping data was curve-fitted by a third-order polynomial. The roots of the polynomial were obtained and used as an estimate of the bifurcation speed. In cases where the polynomial had no suitable roots (i.e. real and higher than the current airspeed), no predicted bifurcation speed was logged.
4. When the ratio of the current airspeed to the predicted bifurcation speed exceeded 80%, the flutter test was stopped. The latest value of the estimated bifurcation speed was taken to be the critical condition.

Fig. 18 shows the variation of the averaged damping criterion obtained throughout the test, The bifurcation speed predictions are tabulated in Table 1. It can be seen that the ratio V_i/V_c exceeded 80% at 31 m/s, at which the predicated
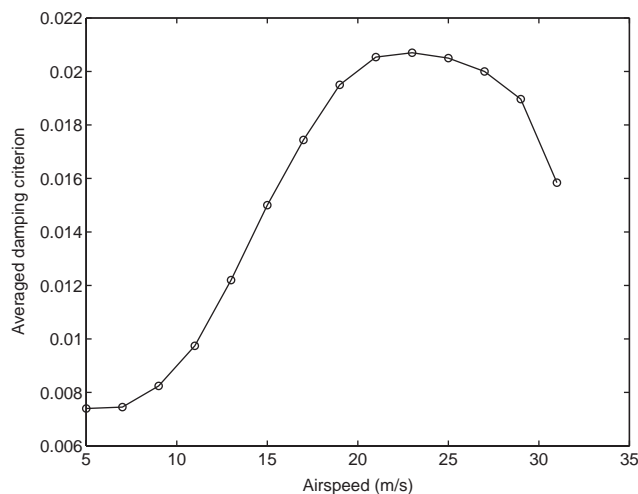
Fig. 18. Variation of averaged damping criterion with airspeed during simulated flutter test.

Table 1
Bifurcation speed estimates, Hancock model with cubic nonlinearity

Current airspeed, V_i (m/s)	Bifurcation speed estimate, V_c (m/s)	V_i/V_c
9	13.07	0.69
11	25.48	0.43
13	18.00	0.72
15	27.88	0.54
17	41.51	0.59
19	N/A	N/A
21	35.76	0.59
23	32.24	0.71
25	34.44	0.73
27	36.10	0.75
29	36.76	0.79
31	38.02	0.82

bifurcation speed was 38.02 m/s. The bifurcation plot of Fig. 15 shows that the true bifurcation speed is 38 m/s, thus demonstrating that the application of the time-varying RFP method can indeed predict the bifurcation speed from sub-critical data.

4.2. Hancock model with freeplay stiffness

The freeplay function applied to the control surface spring of the Hancock model was of the form shown in Fig. 6. The inner stiffness K_1 was equal to 0, the outer stiffness K_2 was chosen as twice the linear stiffness and the width of the freeplay region, δ was $2°$.

Freeplay stiffness is a destabilizing nonlinearity and causes the Hancock model to behave in a highly nonlinear manner. The responses contain a large number of frequencies at irregular intervals and at large separations. Additionally, there are regions in the parameter space where chaotic pockets can occur. A sample impulse response of the control surface is plotted in Fig. 19, demonstrating highly irregular, a periodic behaviour. Nevertheless, the RFP procedure can extract the correct frequencies from the STFT. In Fig. 20 the STFT of the response in Fig. 19 is plotted. The STFT reveals that, between 0 and 3 s, there is a large number of frequency components while, after 4 s only two frequencies are visible. The RFP procedure provides the same frequency information, as shown in Fig. 21.

Fig. 22 shows the bifurcation diagram for the Hancock model with freeplay stiffness in the control surface. The following stability regions can be distinguished:

 (i) 0–15 m/s: the response is decaying;
 (ii) 15–16 m/s: the system exhibits chaotic behaviour; depending on the airspeed the response may be either decaying or a chaotic limit cycle, i.e. a limit cycle with band-limited amplitude; this type of response is sometimes called 'narrow band chaos' (Moon, 1992);
 (iii) 16–44 m/s: period-3 limit cycle;
 (iv) > 44 m/s: flutter.

Fig. 23 shows the damping ratio variation with airspeed. The increased level of noise in the figure is due to the severity of the nonlinear behaviour of the system with freeplay. As mentioned earlier, limit cycle oscillations first appear at 15 m/s, at which point the damping ratios become zero. However, unlike the previous case (cubic nonlinearity), the sub-critical behaviour of the damping ratio plot does not emulate the linear behaviour. Two components with increasing damping ratio can be distinguished, but there is no critical component. Hence, the sub-critical results suggest that the motion becomes increasingly stable with increasing airspeed until instability is suddenly encountered.

The frequency plot of Fig. 24 reveals another aspect of the problem of curve-fitting the response of the system with freeplay stiffness. Since freeplay stiffness in the freeplay region is zero, the stiffness of the control surface in that region is exclusively aerodynamic, which happens to be of much smaller magnitude than the stiffness required to prevent the occurrence of static divergence. Hence, the Hancock wing is diverged at low response amplitudes and, effectively, the control surface degree of freedom has no natural frequency. The two sub-critical frequency components in Fig. 24
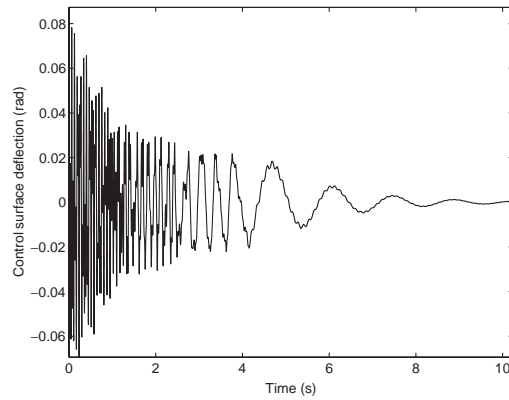
Fig. 19. Example of control surface impulse response from Hancock model with freeplay stiffness.
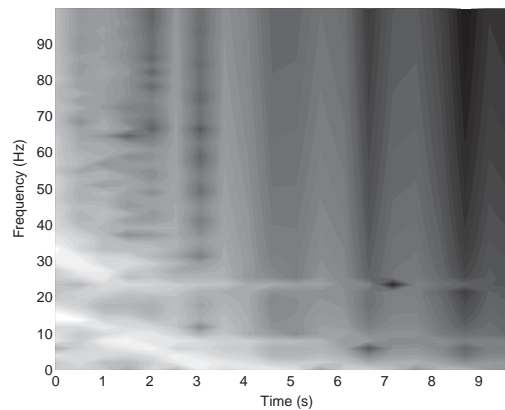
Fig. 20. STFT of response in Fig. 19.
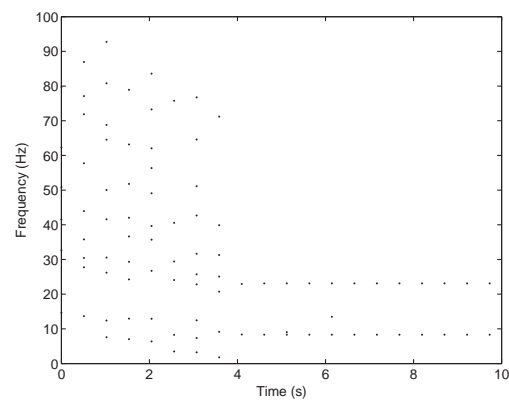
Fig. 21. Frequencies from RFP curve-fit of response in Fig. 19.

represent the wing torsion and wing bending only. The critical degree of freedom does not appear in either the frequency or damping plots.

The particular form of the damping plot for this example (Fig. 23) suggests that it is impossible to use sub-critical damping data to obtain an estimate of the bifurcation airspeed in the presence of freeplay stiffness nonlinearity.
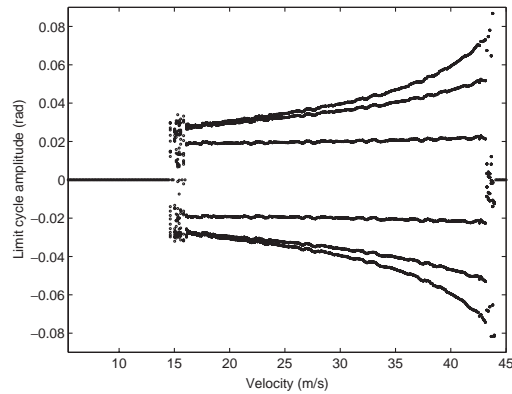
Fig. 22. Bifurcation plot for Hancock model with freeplay stiffness.
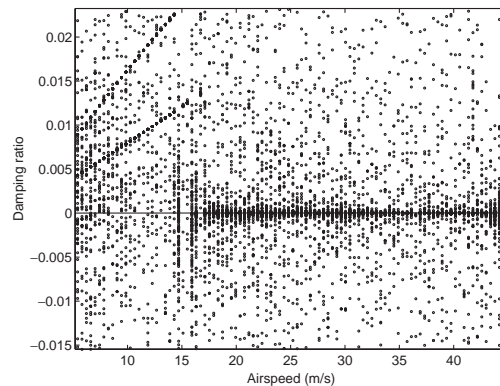
Fig. 23. Time-varying RFP damping plot for Hancock model with freeplay stiffness.
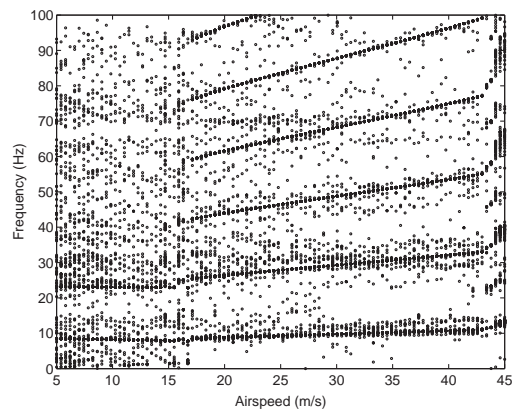
Fig. 24. Time-varying RFP frequency plot for Hancock model with freeplay stiffness.

4.3. CFD 2-dof airfoil model with transonic unsteady aerodynamics

The final example presented in this work concerns a 2-dof airfoil in transonic flow. In this case, there are no structural nonlinearities; the aerodynamic forces are nonlinear. The main effects of this type of nonlinearity are static divergence and bifurcations to limit-cycle behaviour, both of which phenomena are sometimes combined. For an overview of the effects of transonic aerodynamics on flexible aircraft see reference (Anderson, 1995).
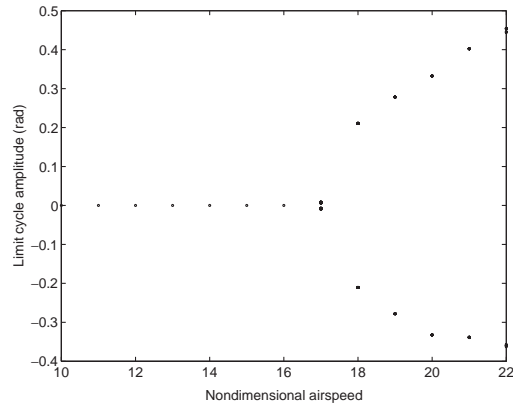
Fig. 25. Bifurcation plot for CFD model.
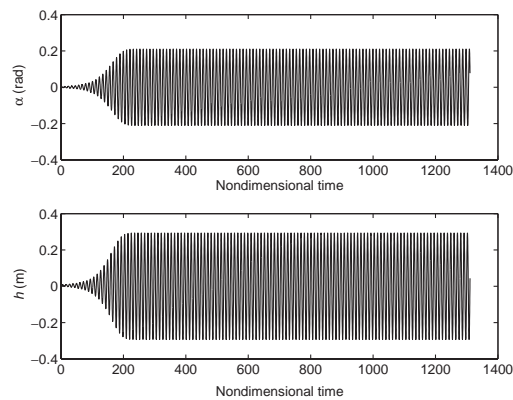
Fig. 26. Pitch (upper plot) and plunge (lower plot) impulse response of CFD model at $U^* = 18$.
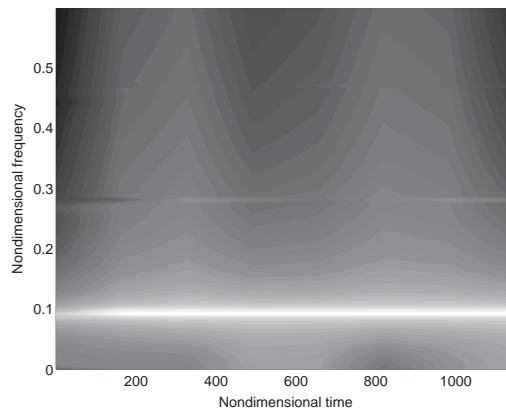
Fig. 27. Short time Fourier transform of pitch response in Fig. 26.

CFD-based transonic aeroelastic computations are becoming increasingly possible within the aeroelastic community, as witnessed by recent publications such as Guillot and Friedmann (2001). In Friedmann (1999), transonic aeroelastic simulation is referred to as '... the *holy grail* of modern aeroelasticity'.

As mentioned earlier, the CFD solution used for the present work was obtained using the Glasgow PMB 2D code. The main governing parameters are Mach number, airspeed and initial conditions. The test-case chosen for the

application of the RFP method concerned a constant Mach number of 0.8 with a variable value of the nondimensional airspeed $\bar{U} = 40U/b\omega_\alpha$, where U is the true airspeed, b is the half-chord and ω_α is the frequency in pitch. The bifurcation diagram for this particular test-case is shown in Fig. 25. The response is decaying up to an airspeed of $\bar{U} = 17$ where period-1 limit cycles appear for the first time. The system flutters at airspeeds higher than $\bar{U} = 22$. The bifurcation diagram is insensitive to initial conditions.
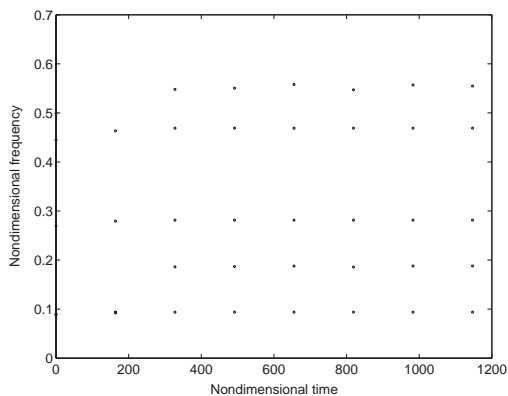
Fig. 28. Frequencies from RFP curve-fit of pitch response in Fig. 26.
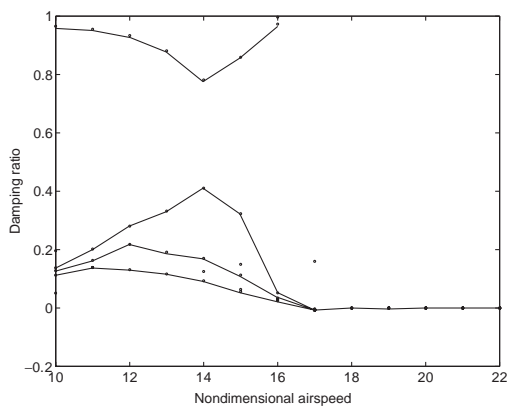
Fig. 29. Time-varying RFP damping plot for CFD model.
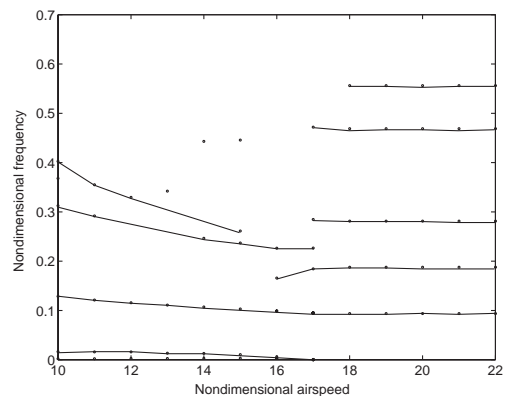
Fig. 30. Time-varying RFP frequency plot for CFD model.

A sample impulse response of both degrees of freedom is plotted in Fig. 26 for $\bar{U} = 18$. It can be seen that the system admits a period-1 limit cycle. The STFT plot of the pitch degree of freedom (Fig. 27) reveals the existence of one base frequency at $\bar{\omega} = 0.9$ and a third-order harmonic component at $\bar{\omega} = 2.7$. It should be noted that $\bar{\omega}$ is a nondimensional frequency. The time-varying RFP analysis for the same signal reveals the existence of a few more harmonic components. Fig. 28 shows the frequency variation with time obtained by means of the RFP procedure. Apart from the first and third harmonics, second, fifth and sixth components are also visible at $\bar{\omega} = 1.8$, 4.5 and 5.4, respectively. Nevertheless, these additional components contain very little energy, which is the reason for their absence from the STFT plot.

Figs. 29 and 30 show the damping and frequency variation with airspeed for the CFD model, obtained through the use of the RFP technique. Both plots were curve-fitted by hand in order to demonstrate the damping and frequency trends more clearly. This procedure was dictated by the fact that the integration of the CFD model is very computationally intensive and, hence, it is impractical to run the same number of simulations as with the earlier examples. Nevertheless, the curve-fit consisted of joining-up adjacent points by hand hence the results were not altered in any way. A very similar approach is used in many flight flutter tests (Kehoe, 1995).

In the damping plot of Fig. 29 there are four curves, three of which behave like classical critical flutter curves. The fourth damping component accounts for the fact that there is a certain amount of static divergence in the impulse responses of the CFD model. The divergence is significant at sub-critical conditions but becomes negligible at airspeeds higher than $\bar{U} = 16$. Hence, at sub-critical flight regimes, there is always a component with a damping ratio of almost 1, i.e. if the corresponding eigenvalue is denoted by λ, $|\Re(\lambda)| \gg |\mathscr{I}(\lambda)|$ and the contribution of this eigenvalue to the system response is mainly rigid-body. The same eigenvalue can be observed in the frequency plot of Fig. 30 where, at sub-critical speeds, there is a component whose frequency is almost zero, again denoting nonoscillatory motion.

After the Hopf bifurcation occurs at $\bar{U} = 17$, the damping of all the components becomes zero while there are five frequency components, as discussed earlier. Nevertheless, the most important feature of the RFP curve-fit of the CFD model is that the sub-critical variation of the damping ratio (especially the two lowest curves) allows for the determination of the critical point from sub-critical data.

4.3.1. Stability Prediction from sub-critical Data

The damping curves of Fig. 29 can be used in order to predict the bifurcation point from sub-critical data, as was done for the Hancock model with cubic nonlinearity. Averaged damping data from sub-critical reduced airspeeds were employed in a simulated flutter test. As was done previously, the averaged damping data were curve-fitted by third-order polynomials at each airspeed and the suitable roots of the polynomials were taken to be the current estimates for the bifurcation condition.

Fig. 31 shows the averaged damping criterion variation with reduced airspeed. The bifurcation speed estimates obtained at each airspeed are shown in Table 2. It can be seen that the ratio of the current airspeed to the predicted bifurcation speed exceeds 80% at a reduced airspeed of 14. Hence, using only sub-critical data from airspeeds at least
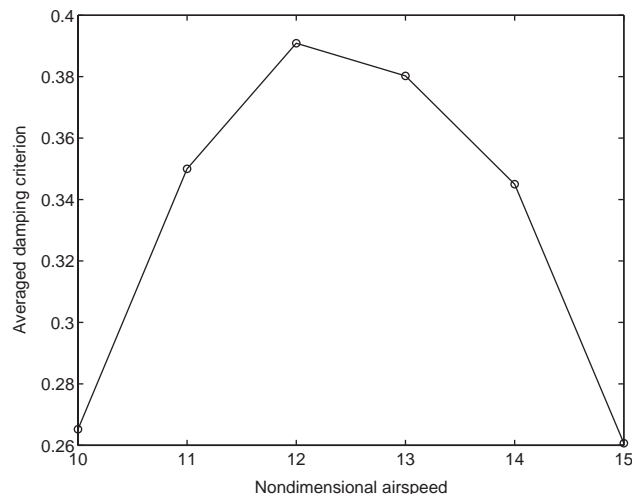
Fig. 31. Variation of averaged damping criterion with airspeed during simulated flutter test for 2-D transonic airfoil.

Table 2
Bifurcation speed estimates, 2-D airfoil in transonic flow

Current airspeed, V_i (m/s)	Bifurcation speed estimate, V_c (m/s)	V_i/V_c
12	15.85	0.76
13	17.60	0.74
14	16.81	0.83
15	16.98	0.88

20% lower than the critical airspeed, the bifurcation condition was pinpointed at a reduced airspeed of 16.81. Since the CFD model was integrated only at integer values of the reduced airspeed, the exact critical airspeed is not known but Figs. 25 and 29 show that it must be between 16 and 17.

It can be concluded that the time-varying RFP method was successfully applied to this 2-D transonic aeroelastic problem in order to predict the bifurcation airspeed from sub-critical impulse response data.

5. Conclusions

A method for the characterization of responses from nonlinear aeroelastic systems has been developed. The technique consists of a frequency curve-fit of short section of the impulse response combined with a time domain signal reconstruction. It is shown that the new methodology can identify frequency components and damping trends for both decaying and limit-cycle responses of aeroelastic systems containing certain types of nonlinearity. Additionally, the damping trends can be used to predict the airspeed at which a bifurcation will occur from sub-critical data.

The approach is applied to two different simulated aeroelastic systems with three types of aerodynamic and structural nonlinearities. It is shown that, in the presence of stabilizing nonlinearities such as hard cubic springs and transonic aerodynamics, the method is successful in describing harmonic components and predicting critical airspeeds. However, in the presence of destabilizing nonlinearities such as freeplay, the method can fail. The success of the method is dependent on the type of bifurcation caused by the nonlinear functions. The stabilizing nonlinearities considered in this work cause Hopf-type bifurcation to limit cycle oscillations. In these cases the method will successfully predict the bifurcation condition from sub-critical data. However, freeplay stiffness can cause a chaotic bifurcation and, as a consequence, the method fails when applied to an aeroelastic system with freeplay in the control surface.

References

Allen, J.B., Rabiner, L.R., 1977. A unified approach to short-time Fourier analysis and synthesis. Proceedings of the IEEE 65, 1558–1564.

Anderson, J., 1995. Conjectures on new transonic aeroelastic phenomena. In: Proceedings of the CEAS International Forum on Aeroelasticity and Structural Dynamics, Manchester, UK.

Badcock, K.J., Sim, G., Richards, B.E., 1995. Aeroelastic studies using transonic flow CFD modelling. In: Proceedings of the CEAS International Forum on Aeroelasticity and Structural Dynamics, Manchester, UK.

Dimitriadis, G., Cooper, J.E., 1999. Limit cycle oscillation control and suppression. Aeronautical Journal 103, 257–263.

Dimitriadis, G., Cooper, J.E., 2000. Characterization of the behaviour of a simple aeroservoelastic system with control nonlinearities. Journal of Fluids and Structures 14, 1173–1193.

Friedmann, P.P., 1999. Renaissance of aeroelasticity and its future. Journal of Aircraft 35, 105–121.

Géradin, M., Rixen, D., 1997. Mechanical Vibrations. Wiley, Chichester.

Goura, L., Badcock, K., Woodgate, M., Richards, B., 2001a. A data exchange method for fluid-structure interaction problems. Aeronautical Journal 105, 215–221.

Goura, L., Badcock, K., Woodgate, M., Richards, B., 2001b. Implicit method for the time marching analysis of flutter. Aeronautical Journal 105, 199–214.

Guillot, D., Friedmann, P.P., 2001. Fundamental aeroelastic study combining unsteady computational fluid mechanics and adaptive control. Journal of Guidance Control and Dynamics 23, 1117–1126.

Hancock, G.J., Wright, J.R., Simpson, A., 1985. On the teaching of the principles of wing flexure-torsion flutter. Aeronautical Journal 89, 285–305.

Heil, C.E., Walnut, D.F., 1989. Continuous and discrete wavelet transforms. SIAM Review 31, 628–666.

Kehoe, M.W., 1995. A historical overview of flight flutter testing. Paper presented at the 80th meeting of the AGARD Structures and Materials Panel, Rotterdam, The Netherlands.

Kim, S.H., Lee, I., 1996. Aeroelastic analysis of a flexible airfoil with a freeplay non-linearity. Journal of Sound and Vibration 193, 823–846.

Lee, B.H.K., Price, S.J., Wong, Y.S., 1999. Nonlinear aeroelastic analysis of airfoils: bifurcation and chaos. Progress in Aerospace Sciences 35, 205–334.

Levitas, J., Weller, T., Singer, J., 1994. Poincare-like simple cell mapping for non-linear dynamical systems. Journal of Sound and Vibration 176, 641–662.

Liu, L., Wong, Y.S., Lee, B.H.K., 1999. Application of the centre manifold theory in non-linear aeroelasticity. Journal of Sound and Vibration 234, 641–659.

Mastroddi, F., Bettoli, A., 1999. Wavelet analysis for Hopf bifurcations with aeroelastic applications. Journal of Sound and Vibration 225, 887–913.

Moon, F.C., 1992. Chaotic and Fractal Dynamics—An Introduction for Applied Scientists and Engineers. Wiley, New York.

Price, S.J., Alighanbari, H., Lee, B.H.K., 1995. The aeroelastic behaviour of a two-dimensional airfoil with bilinear and cubic structural nonlinearities. Journal of Fluids and Structures 9, 175–193.

Price, S.J., Lee, B.H.K., Alighanbari, H., 1994. Postinstability behaviour of a two-dimensional airfoil with a structural nonlinearity. Journal of Aircraft 31, 1395–1401.

Raghothama, A., Narayanan, S., 1999. Non-linear dynamics of a two-dimensional airfoil by incremental harmonic balance method. Journal of Sound and Vibration 226, 493–517.

Richardson, M., Formenti, D.L., 1982. Parameter estimation from frequency response measurements using rational fraction polynomials. In: Proceedings of the 1st International Modal Analysis Conference, Orlando, FL.